A Pre-Scaled Multiplicative Regularized Gauss-Newton Inversion

Puyan Mojabi and Joe LoVetri

Abstract—A pre-scaled multiplicative regularized Gauss-Newton inversion algorithm is proposed which utilizes *a priori* information about the expected ratio between the average magnitude of the real and imaginary parts of the true contrast as well as the expected ratio between the average magnitude of the gradient of the real and imaginary parts of the true contrast. Using both synthetically and experimentally collected data sets, we show that this pre-scaled inversion algorithm is successful in reconstructing both real and imaginary parts of the contrast when there is a large imbalance between the average magnitude of these two parts where the standard multiplicative regularized Gauss-Newton inversion algorithm fails. We further show that the proposed pre-scaled inversion algorithm is robust and does not require the *a priori* information to be exact.

Index Terms—Microwave tomography, Gauss-Newton inversion, Regularization.

I. INTRODUCTION

IN microwave tomography (MWT), the goal is to reconstruct the complex permittivity of the object of interest (OI) using scattered field data collected outside the OI. Different iterative algorithms such as contrast source inversion [1]–[6], Gauss-Newton inversion [7]–[11], and stochastic optimization methods [12]–[14] have been utilized to handle the nonlinearity of the problem. In conjunction with these iterative techniques, different regularization techniques such as additive [15], [16], multiplicative [3], [9], [10], and projection-based regularization techniques [17], [18] have been used to treat the ill-posedness of the problem. Microwave tomography is of interest for various applications such as oil and gas-multiphase-flow imaging [19] and biomedical imaging [20]–[22]. In some applications of MWT, the magnitude of the real and imaginary parts of the OI's permittivity can considerably be out of balance [23]. For example, in biomedical imaging, the real part of the permittivity can be much larger than the imaginary part. As a result of this imbalance, *blind* inversion algorithms inadvertently favor the reconstruction of the real part over the imaginary part. This imbalance usually results in an oscillatory reconstruction of the imaginary part of the permittivity. To enhance the imaginary-part reconstruction for these cases, Meaney *et. al.* developed a pre-scaled Gauss-Newton inversion algorithm based on Tikhonov regularization which optimizes over the imaginary part and an scaled version of the real part [23].

In this paper, we present a pre-scaled multiplicative regularized Gauss-Newton inversion algorithm which adjusts the average magnitude of the real and imaginary parts of the OI's electric contrast throughout the inversion algorithm. In this method, the MWT problem is regularized with a weighted L_2-norm total variation multiplicative regularizer which enforces a larger regularization weight on the imaginary-part reconstruction than the real-part reconstruction. As will be shown using synthetically and experimentally collected data sets, the standard multiplicative regularized Gauss-Newton inversion algorithm fails in reconstructing the imaginary part of the contrasts when a large imbalance exists between the average magnitude of the real and imaginary parts. We show that the proposed pre-scaled inversion algorithm is capable of reconstructing both real and imaginary parts of such targets. We further show that the algorithm does not require the *a priori* information to be exact. In general, the proposed algorithm can improve reconstruction results for the applications wherein the real and imaginary parts of the contrast are out of balance such as biomedical imaging applications. Within the framework of this paper, we consider the two-dimensional transverse magnetic (TM) illumination and assume a time factor of $\exp(-j\omega t)$.

II. PROBLEM FORMULATION

Consider a bounded imaging domain $\mathcal{D} \subset \mathbb{R}^2$ containing a non-magnetic OI and a measurement domain $\mathcal{S} \subset \mathbb{R}^2$ outside of the object of interest. The imaging domain $\mathcal{D}$ is immersed in a known non-magnetic homogeneous background medium with the relative complex permittivity of ϵ_b. Denoting the unknown relative complex permittivity of the OI at the position $\boldsymbol{q} \in \mathcal{D}$ by $\epsilon_r(\boldsymbol{q})$, the complex electric contrast function is defined as

$$\chi(\boldsymbol{q}) \triangleq \frac{\epsilon_r(\boldsymbol{q}) - \epsilon_b}{\epsilon_b}. \tag{1}$$

In MWT, the OI is successively interrogated with a number of known incident fields E_t^{inc}, where $t = 1, \cdots, T_x$. Interaction of the incident field E_t^{inc} with the OI results in the total field E_t. The scattered electric field E_t^{scat} is then defined as the difference between the total and incident electric fields corresponding to the tth transmitter; i.e., $E_t^{\text{scat}} \triangleq E_t - E_t^{\text{inc}}$. The total and incident electric fields are then measured by some receiver antennas located on $\mathcal{S}$. Thus, the scattered electric field corresponding to the tth transmitter is known on $\mathcal{S}$ and denoted by $E_{\text{meas},t}^{\text{scat}}$. The MWT problem may then be formulated as the minimization over χ of the least-squares

data misfit cost-functional

$$\mathcal{C}^{\text{LS}}(\chi) = \eta_{\mathcal{S}} \sum_{t=1}^{T_x} \left\| E_t^{\text{scat}}(\chi) - E_{\text{meas},t}^{\text{scat}} \right\|_{\mathcal{S}}^2 \qquad (2)$$

where $E_t^{\text{scat}}(\chi)$ is the simulated scattered field at the observation points corresponding to the contrast χ and the tth transmitter, and $\|.\|_{\mathcal{S}}$ denotes the 2-norm on $\mathcal{S}$. The weighting $\eta_{\mathcal{S}}$ is chosen to be $\eta_{\mathcal{S}} = \left(\sum_{t=1}^{T_x} \left\| E_{\text{meas},t}^{\text{scat}} \right\|_{\mathcal{S}}^2 \right)^{-1}$.

III. MULTIPLICATIVE REGULARIZED GAUSS-NEWTON INVERSION (MR-GNI)

The Gauss-Newton inversion (GNI) method is based on the Newton optimization, but ignores the second derivative of the scattered electric field with respect to the contrast function. That is, the scattered field due to the contrast $\chi + \Delta\chi$ is approximated as,

$$E_t^{\text{scat}}(\chi + \Delta\chi) \approx E_t^{\text{scat}}(\chi) + \frac{\partial E_t^{\text{scat}}}{\partial \chi}(\Delta\chi). \qquad (3)$$

This approximation, which we refer to as the GNI approximation, utilizes only the first two terms of the Taylor's expansion. As far as the updating scheme is concerned, the contrast at the nth iteration of the GNI method is updated as $\chi_{n+1} = \chi_n + \nu_n \Delta\chi_n$ where χ_n is the predicted contrast at the nth iteration, ν_n is an appropriate step-length, and $\Delta\chi_n$ is the correction.

To treat the ill-posedness of the problem, the data misfit cost-functional may be regularized using different regularization techniques [24]. Herein, we regularize $\mathcal{C}^{\text{LS}}$ by the weighted L_2-norm total variation multiplicative regularizer. That is, at the nth iteration of the inversion algorithm, we minimize [9], [10], [24]

$$\mathcal{C}_n(\chi) = \mathcal{C}^{\text{LS}}(\chi)\mathcal{C}_n^{\text{MR}}(\chi). \qquad (4)$$

The multiplicative regularization term is given as

$$\mathcal{C}_n^{\text{MR}}(\chi) = \int_{\mathcal{D}} b_n^2(\boldsymbol{q})(|\nabla\chi(\boldsymbol{q})|^2 + \alpha_n^2)d\boldsymbol{q} \qquad (5)$$

where the gradient ∇ is taken with respect to the position vector $\boldsymbol{q}$. Denoting the area of the imaging domain by A, the weighting function b_n is given as

$$b_n(\boldsymbol{q}) = A^{-\frac{1}{2}}(|\nabla\chi_n(\boldsymbol{q})|^2 + \alpha_n^2)^{-\frac{1}{2}}. \qquad (6)$$

The choice of the steering parameter α_n^2 is described below. It is worth noting that this multiplicative regularizer provides an edge-preserving regularization where the regularization weight is chosen by the algorithm itself [24].

In the discrete setup, we discretize the imaging domain $\mathcal{D}$ into N cells using 2D pulse basis functions. Thus, the contrast function is represented by the complex vector $\underline{\chi} \in \mathbb{C}^N$. Assuming the number of measured data to be M, the measured scattered data on the discrete measurement domain $\mathcal{S}$ is denoted by the complex vector $\underline{E}_{\text{meas}}^{\text{scat}} \in \mathbb{C}^M$. The vector $\underline{E}_{\text{meas}}^{\text{scat}}$ is the stacked version of the measured scattered fields for each transmitter. The vector $\underline{E}^{\text{scat}} \in \mathbb{C}^M$ is then formed by stacking the discrete forms of $E_t^{\text{scat}}(\chi_n)$. The matrix $\underline{\boldsymbol{J}}_{t,n}$ represents

the discrete form of the derivative of the scattered field with respect to the contrast and evaluated at $\chi = \chi_n$. That is, it represents the discrete form of $\frac{\partial E_t^{\text{scat}}}{\partial \chi}\big|_{\chi_n}$. The Jacobian matrix $\underline{\boldsymbol{J}}_n \in \mathbb{C}^{M \times N}$ is then formed by stacking $\underline{\boldsymbol{J}}_{t,n}$ matrices where $t = 1, \cdots, T_x$. The positive parameter α_n^2 is chosen to be $\mathcal{C}^{\text{LS}}(\underline{\chi}_n)/\Delta A$ where ΔA is the area of a single cell in the uniformly discretized domain $\mathcal{D}$ [9], [10], [24].

Minimizing $\mathcal{C}_n(\underline{\chi})$ over the complex vector $\underline{\chi}$, the complex correction vector $\Delta\underline{\chi}_n$ may be found from [9], [10], [24]

$$(\underline{\boldsymbol{J}}_n^H \underline{\boldsymbol{J}}_n - \beta_n \underline{\boldsymbol{\mathcal{L}}}_n)\Delta\underline{\chi}_n = \underline{\boldsymbol{J}}_n^H \underline{d}_n + \beta_n \underline{\boldsymbol{\mathcal{L}}}_n \underline{\chi}_n \qquad (7)$$

where the discrepancy vector $\underline{d}_n$ is given as $\underline{d}_n = \underline{E}_{\text{meas}}^{\text{scat}} - \underline{E}_n^{\text{scat}}$ and $\beta_n = \|\underline{d}_n\|^2$. The regularization operator $\underline{\boldsymbol{\mathcal{L}}}_n$ represents the discrete form of the operator $\nabla \cdot b_n^2 \nabla$ where $\nabla\cdot$ is the divergence operator. We note that the weighted Laplacian operator, $\nabla \cdot b_n^2 \nabla$, provides edge-preserving characteristics for the inversion algorithm [10]. This completes the brief explanation of the MR-GNI method.

IV. PRE-SCALED MR-GNI (PSMR-GNI)

Assume that there exist two pieces of *a priori* information about the OI: (*i*) the expected ratio between the the average magnitude of the real and imaginary parts of the OI's contrast, and (*ii*) the expected ratio between the the average magnitude of the gradient of the real and imaginary parts of the OI's contrast. Denoting the real and imaginary parts of the OI's contrast by $\chi_{\text{R}} = \text{Re}(\chi)$ and $\chi_{\text{I}} = \text{Im}(\chi)$, respectively, we suppose that the average magnitude of χ_{R} is approximately $Q \in \mathbb{R}$ times larger than the average magnitude of χ_{I}. We further assume that the average magnitude of $\nabla\chi_{\text{R}}$ is approximately $Q_{\text{TV}} \in \mathbb{R}$ times larger than the average magnitude of $\nabla\chi_{\text{I}}$.

To incorporate these two pieces of *a priori* information into the inversion algorithm, we take three main steps. First, we formulate the problem in the real-domain as opposed to the complex-domain formulation presented in Section III. Second, we utilize a pre-scaled weighted L_2-norm total variation multiplicative regularizer which enforces a similar weight on the average magnitude of $\nabla\chi_{\text{R}}$ and $\nabla\chi_{\text{I}}$. Third, we balance the real and imaginary parts of the correction vector at the updating stage of the algorithm.

Formulating the optimization problem in terms of the real and imaginary parts of the contrast; i.e., χ_{R} and χ_{I}, at the nth iteration, we minimize the cost-functional

$$\tilde{\mathcal{C}}_n(\chi_{\text{R}}, \chi_{\text{I}}) = \tilde{\mathcal{C}}^{\text{LS}}(\chi_{\text{R}}, \chi_{\text{I}})\mathcal{C}_n^{\text{PSMR}}(\chi_{\text{R}}, \chi_{\text{I}}). \qquad (8)$$

where $\tilde{\mathcal{C}}^{\text{LS}}(\eta, \gamma)$ is equal to $\mathcal{C}^{\text{LS}}(\eta + j\gamma)$ assuming that η and γ belong to the L_2 space of real functions defined on $\mathcal{D}$. The pre-scaled multiplicative regularizer $\mathcal{C}_n^{\text{PSMR}}(\chi_{\text{R}}, \chi_{\text{I}})$ is chosen as

$$\mathcal{C}_n^{\text{PSMR}}(\chi_{\text{R}}, \chi_{\text{I}}) = \int_{\mathcal{D}} (b_n^{\text{PS}})^2 (|\nabla\chi_{\text{R}}|^2 + Q_{\text{TV}}^2 |\nabla\chi_{\text{I}}|^2 + \alpha_n^2)d\boldsymbol{q} \qquad (9)$$

where

$$b_n^{\text{PS}}(\boldsymbol{q}) = A^{-\frac{1}{2}}(|\nabla\chi_{\text{R},n}(\boldsymbol{q})|^2 + Q_{\text{TV}}^2 |\nabla\chi_{\text{I},n}(\boldsymbol{q})|^2 + \alpha_n^2)^{-\frac{1}{2}} \qquad (10)$$

(a) Re(ϵ_r) (b) Im(ϵ_r)

(c) Re(ϵ_r) (d) Im(ϵ_r)
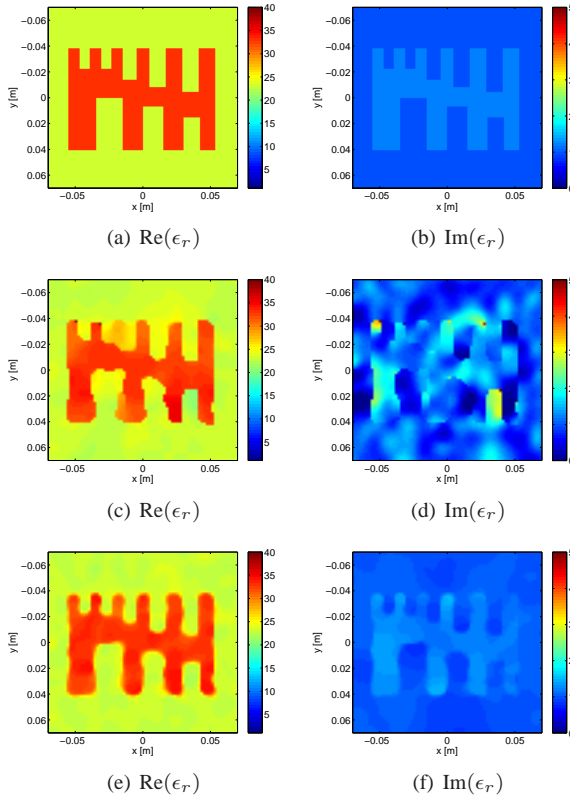
(e) Re(ϵ_r) (f) Im(ϵ_r)

Fig. 1. (a)-(b) Real and imaginary parts of the first synthetic target's relative complex permittivity, (c)-(d) its reconstruction using MR-GNI, and (e)-(f) its reconstruction using PSMR-GNI with $Q = Q_{TV} = 10$.

(a) Re(ϵ_r) (b) Im(ϵ_r)

(c) Re(ϵ_r) (d) Im(ϵ_r)
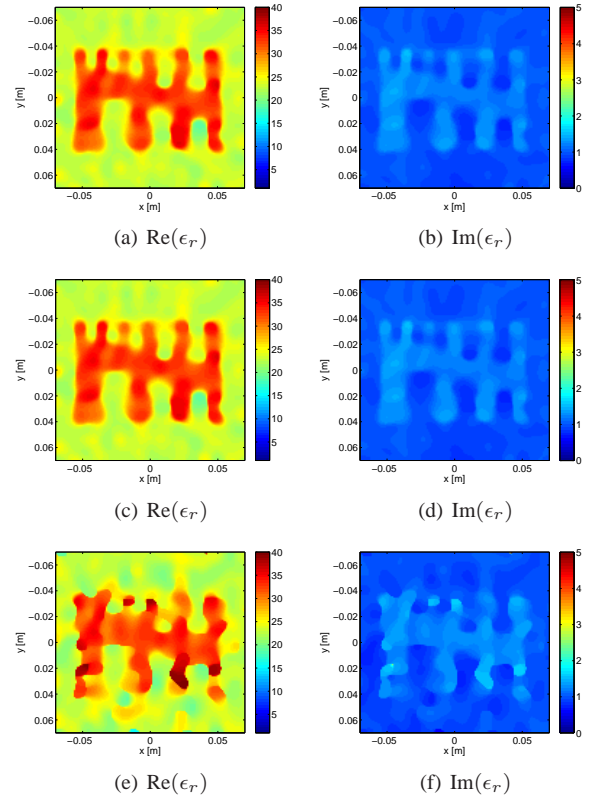
(e) Re(ϵ_r) (f) Im(ϵ_r)

Fig. 2. The reconstructed relative complex permittivity of the first synthetic target using (a)-(b) PSMR-GNI with $Q = Q_{TV} = 20$, (c)-(d) PSMR-GNI with $Q = Q_{TV} = 40$, and (e)-(f) PSMR-GNI with $Q = Q_{TV} = 60$.

and $\chi_{R,n}$ and $\chi_{I,n}$ are the real and imaginary parts of the predicted contrast at the nth iteration of the GNI algorithm. As can be seen, the weight of $|\nabla \chi_I|$ is chosen to be Q_{TV} times more than that of $|\nabla \chi_R|$ so as to balance the contribution of these two quantities in the multiplicative regularizer. We note that when Q_{TV} is chosen to be 1, $\mathcal{C}_n^{\text{PSMR}}$ will be the same as $\mathcal{C}_n^{\text{MR}}$ given in (5).

Usually, there is no *a priori* information about the ratio between the average magnitude of the gradient of the real and imaginary parts of the contrast. However, from our numerical experiments, we have found when there is a *large* imbalance between the average magnitude of χ_R and χ_I, there is a similar imbalance between the average magnitude of $\nabla \chi_R$ and $\nabla \chi_I$. Thus, for realistic targets, we can set Q_{TV} equal to Q. Although we formulate the problem in terms of Q and Q_{TV}, we set $Q_{TV} = Q$ in all the numerical results, unless otherwise stated. It is useful to keep them separate in the derivation of the algorithm so that their individual effect on the final algorithm can be clearly identified.

In the discrete domain, the real-valued correction vectors, $\Delta \underline{\chi}_{R,n} \in \mathbb{R}^N$ and $\Delta \underline{\chi}_{I,n} \in \mathbb{R}^N$, may be found by solving

$$\underline{\boldsymbol{H}}_{\text{GN},n} \begin{bmatrix} \Delta \underline{\chi}_{R,n} \\ \Delta \underline{\chi}_{I,n} \end{bmatrix} = -\underline{g}_n \tag{11}$$

where $\underline{g}_n$ is the gradient vector at the nth iteration of the inversion algorithm. The matrix $\underline{\boldsymbol{H}}_{\text{GN},n}$ represents the approximate form of the Hessian matrix, $\underline{\boldsymbol{H}}_n$, calculated using the GNI

approximation, (3). The conjugate gradient (CG) algorithm is used to solve (11). However, due to the imbalance between $\Delta \underline{\chi}_{R,n}$ and $\Delta \underline{\chi}_{I,n}$, we first equilibrate this linear system of equations utilizing the scheme used by Meaney *et. al.* [23]: we introduce a dummy variable $\chi_R^{\text{PS}} = \chi_R / Q$; thus, balancing the average magnitude of χ_R^{PS} and χ_I. We then optimize over χ_R^{PS} and χ_I. Thus, instead of solving (11), we solve

$$\underline{\boldsymbol{H}}_{\text{GN},n}^{\text{PS}} \begin{bmatrix} \Delta \underline{\chi}_{R,n}^{\text{PS}} \\ \Delta \underline{\chi}_{I,n} \end{bmatrix} = -\underline{g}_n^{\text{PS}} \tag{12}$$

where the pre-scaled gradient vector is given as

$$\underline{g}_n^{\text{PS}} = \begin{bmatrix} Q \frac{\partial \tilde{\mathcal{C}}}{\partial \underline{\chi}_R} \Big|_{\underline{\chi} = \underline{\chi}_n} \\ \frac{\partial \tilde{\mathcal{C}}}{\partial \underline{\chi}_I} \Big|_{\underline{\chi} = \underline{\chi}_n} \end{bmatrix}, \tag{13}$$

and the matrix $\underline{\boldsymbol{H}}_{\text{GN},n}^{\text{PS}}$ is the pre-scaled Hessian matrix,

$$\underline{\boldsymbol{H}}_n^{\text{PS}} = \begin{bmatrix} Q^2 \frac{\partial^2 \tilde{\mathcal{C}}}{\partial \underline{\chi}_R \partial \underline{\chi}_R} \Big|_{\underline{\chi} = \underline{\chi}_n} & Q \frac{\partial^2 \tilde{\mathcal{C}}}{\partial \underline{\chi}_R \partial \underline{\chi}_I} \Big|_{\underline{\chi} = \underline{\chi}_n} \\ Q \frac{\partial^2 \tilde{\mathcal{C}}}{\partial \underline{\chi}_I \partial \underline{\chi}_R} \Big|_{\underline{\chi} = \underline{\chi}_n} & \frac{\partial^2 \tilde{\mathcal{C}}}{\partial \underline{\chi}_I \partial \underline{\chi}_I} \Big|_{\underline{\chi} = \underline{\chi}_n} \end{bmatrix}. \tag{14}$$

calculated under the GNI approximation, (3).

As shown in the Appendix, the pre-scaled gradient vector $\underline{g}_n^{\text{PS}}$ can be conveniently written as

$$-2\eta_S \begin{bmatrix} Q \text{Re} \left(\underline{\boldsymbol{J}}_n^H \underline{d}_n \right) + Q \beta_n \underline{\boldsymbol{\mathcal{L}}}_n^{\text{PS}} \underline{\chi}_{R,n} \\ \text{Im} \left(\underline{\boldsymbol{J}}_n^H \underline{d}_n \right) + Q_{TV}^2 \beta_n \underline{\boldsymbol{\mathcal{L}}}_n^{\text{PS}} \underline{\chi}_{I,n} \end{bmatrix}, \tag{15}$$

(a) Re(ϵ_r) (b) Im(ϵ_r)

(c) Re(ϵ_r) (d) Im(ϵ_r)

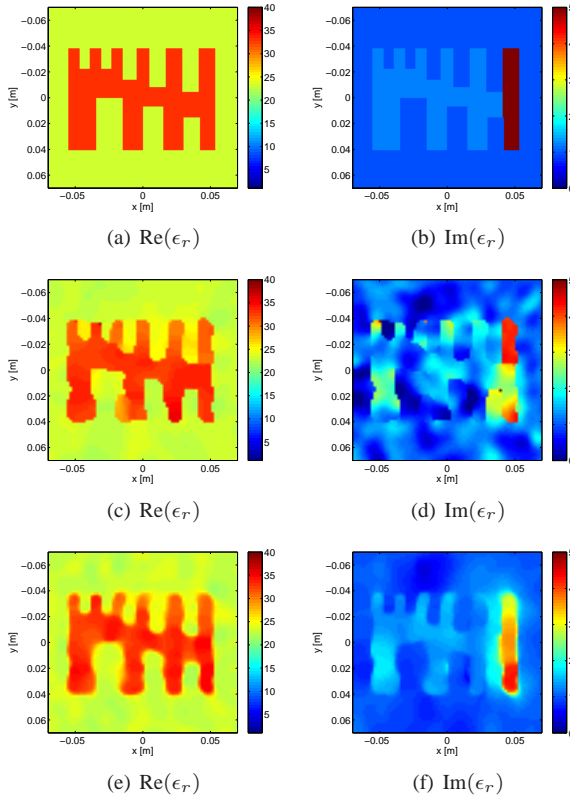(e) Re(ϵ_r) (f) Im(ϵ_r)

Fig. 3. (a)-(b) Real and imaginary parts of the second synthetic target's relative complex permittivity, (c)-(d) its reconstruction using MR-GNI, and (e)-(f) its reconstruction using PSMR-GNI with $Q = Q_{\text{TV}} = 5$.
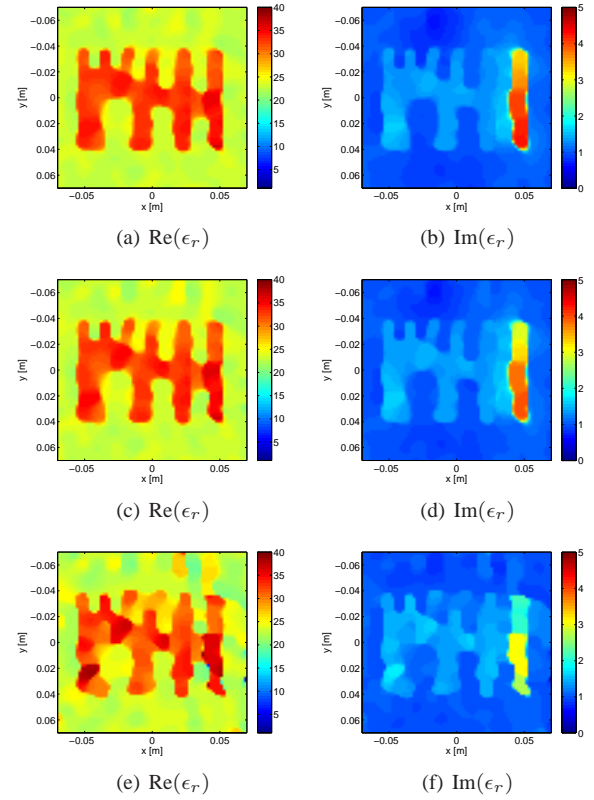
(a) Re(ϵ_r) (b) Im(ϵ_r)

(c) Re(ϵ_r) (d) Im(ϵ_r)

(e) Re(ϵ_r) (f) Im(ϵ_r)

Fig. 4. The reconstructed relative complex permittivity of the second synthetic target using (a)-(b) PSMR-GNI with $Q = Q_{\text{TV}} = 10$, (c)-(d) PSMR-GNI with $Q = Q_{\text{TV}} = 13$, and (e)-(f) PSMR-GNI with $Q = Q_{\text{TV}} = 20$.

and the matrix $\underline{\boldsymbol{H}}^{\text{PS}}_{\text{GN},n}$ as

$$2\eta_{\mathcal{S}} \begin{bmatrix} Q^2\text{Re}(\boldsymbol{J}_n^H \boldsymbol{J}_n) - Q^2\beta_n\boldsymbol{\mathcal{L}}_n^{\text{PS}} & -Q\text{Im}(\boldsymbol{J}_n^H \boldsymbol{J}_n) \\ Q\text{Im}(\boldsymbol{J}_n^H \boldsymbol{J}_n) & \text{Re}(\boldsymbol{J}_n^H \boldsymbol{J}_n) - Q_{\text{TV}}^2\beta_n\boldsymbol{\mathcal{L}}_n^{\text{PS}} \end{bmatrix}.$$ (16)

The operator $\boldsymbol{\mathcal{L}}_n^{\text{PS}}$ is the discrete form of the operator '$\nabla \cdot (b_n^{\text{PS}})^2 \nabla$'. Once $\Delta\underline{\chi}_{\text{R},n}^{\text{PS}}$, and $\Delta\underline{\chi}_{\text{I},n}$ are found, the real and imaginary parts of the contrast are updated as $\underline{\chi}_{\text{R},n+1} = \underline{\chi}_{\text{R},n} + \nu_n Q\Delta\underline{\chi}_{\text{R},n}^{\text{PS}}$ and $\underline{\chi}_{\text{I},n+1} = \underline{\chi}_{\text{I},n} + \nu_n\Delta\underline{\chi}_{\text{I},n}$.

As far as the regularization is concerned, the edge-preserving characteristics of the regularization operators, $\boldsymbol{\mathcal{L}}_n$ in the complex-domain and $\boldsymbol{\mathcal{L}}_n^{\text{PS}}$ in the real-domain, are governed by b_n^2 and $(b_n^{\text{PS}})^2$ respectively [24]. When there is a large imbalance between the average magnitudes of $\nabla\chi_{\text{R},n}$ and $\nabla\chi_{\text{I},n}$, the average magnitude of $\nabla\chi_n$ is dominated by that of $\nabla\chi_{\text{R},n}$. Thus, if the complex-domain formulation is used for such cases, the edge-preserving characteristic of the algorithm is effectively governed only by the magnitude of $\nabla\chi_{\text{R},n}$. However, in the pre-scaled real-domain approach, the magnitude of $\nabla\chi_{\text{I},n}$ can also play a role as long as $\nabla\chi_{\text{R},n}$ and $Q_{\text{TV}}\nabla\chi_{\text{I},n}$ have similar magnitudes, see (10). This explains why we need such a weight in $(b_n^{\text{PS}})^2$. To justify the presence of Q_{TV} in the other factor of the integrand of (9), we note that we want the value of $\mathcal{C}_n^{\text{PSMR}}$ evaluated at $\chi_{\text{R},n}$ and $\chi_{\text{I},n}$ to be 1 at each iteration of the algorithm as the main goal of the optimization is to minimize $\tilde{\mathcal{C}}^{\text{LS}}$ not $\mathcal{C}_n^{\text{PSMR}}$.

We remark that when $Q = Q_{\text{TV}} = 1$, solving (11) is equivalent to solving (7). This can be checked by multiplying the second row of (11) by j and adding that to the first row of (11), and is a verification that optimizing in the real-domain is equivalent to that in the complex-domain. This completes the description of the pre-scaled MR-GNI method to which we refer as the PSMR-GNI method.

Finally, we note that in practical applications, there is usually some *a priori* information about the dielectric properties of the object being imaged. For examples, in biomedical applications, we usually know the average dielectric properties of the biological tissues being imaged. Noting that the dielectric properties of the background medium are also known, the average contrast of the tissues being imaged is available which can be used in setting the value of Q. However, it is usually not straightforward to have *a priori* information which can be used in setting the value of Q_{TV}. As explained earlier in this Section, we can set the value of Q_{TV} equal to Q in the practical cases where there is a large imbalance between the real and imaginary parts of the contrast.

V. SYNTHETIC DATA RESULTS

We first consider the target shown in Fig. 1(a) and (b) which has the same geometry as the target used in [25] and [26] for a resolution test study. This target has features of various dimensions ranging from 8 mm to 20 mm. The relative complex permittivity of the target is $33 + j1.2$ and that of the background medium is $23 + j$ at the frequency of operation which is chosen to be 2 GHz. The corresponding contrast

(a) Dielectric phantom

(b) Re(ϵ_r)

(c) Im(ϵ_r)
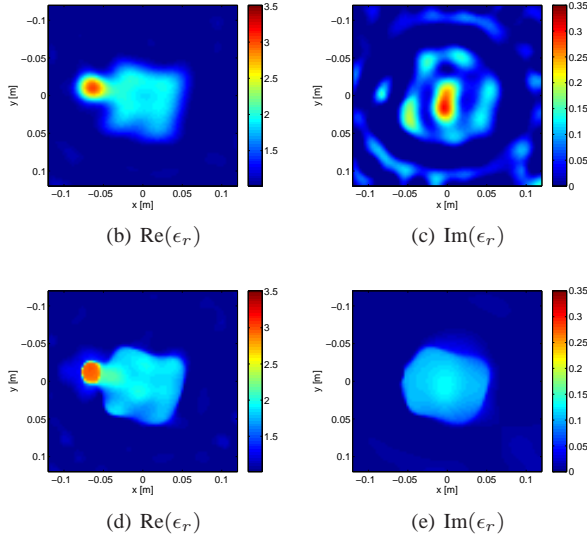

(d) Re(ϵ_r)

(e) Im(ϵ_r)
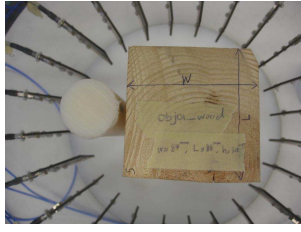
Fig. 5. (a) Dielectric phantom consisting of nylon and wooden cylinders, (b)-(c) its reconstruction using MR-GNI, and (d)-(e) its reconstruction using PS-MRGNI with $Q = Q_{TV} = 10$.

(a) Re(ϵ_r)

(b) Im(ϵ_r)

(c) Re(ϵ_r)

(d) Im(ϵ_r)

(e) Re(ϵ_r)

(f) Im(ϵ_r)

Fig. 6. The reconstructed relative complex permittivity of the nylon-wood phantom using (a)-(b) PSMR-GNI with $Q = Q_{TV} = 20$, (c)-(d) PSMR-GNI with $Q = Q_{TV} = 40$, and (e)-(f) PSMR-GNI with $Q = Q_{TV} = 70$.

is about $0.43 - j0.01$ at $f = 2$ GHz; thus, the true ratio between the real and imaginary parts of the OI's contrast is about 40. Noting that the OI is a homogeneous target, the required Q_{TV} is very close to the true value of Q, based on the numerical evaluation of the gradient on the grid. The synthetic scattering data, which includes 16 transmitters and 16 receivers per transmitter, is generated using a grid of 150×150 square pulses in a 0.126×0.126 m^2 square. We have also added 3% RMS additive white noise to the synthetic data set using the formula given in [27]. The imaging domain is chosen to be a 0.14×0.14 m^2 and is discretized into 71×71 square pulses. The inversion of this data set using the MR-GNI method is shown in Fig. 1(c) and (d). As can be seen, the imaginary-part reconstruction is not satisfactory. Moreover, one of the three upper left details of the target is very blurred in the real-part reconstruction. Using the PSMR-GNI method with $Q = Q_{TV} = 10$, both real- and imaginary-part reconstructions, see Fig. 1(e) and (f), are sucessful. The inversion results using the PSMR-GNI method for three more values of Q and Q_{TV} are shown in Fig. 2. As can be seen, the pre-scaled inversions corresponding to $Q = Q_{TV} = 20$ and $Q = Q_{TV} = 40$ are successful in reconstructing the real and imaginary parts of the contrast. However, the pre-scaled inversion begins to deteriorate at $Q = Q_{TV} = 60$. We note that setting $Q_{TV} = 1$ and having $Q = 40$ (and, vice versa) failed to reconstruct the imaginary part of this target (not shown here). Finally, it should
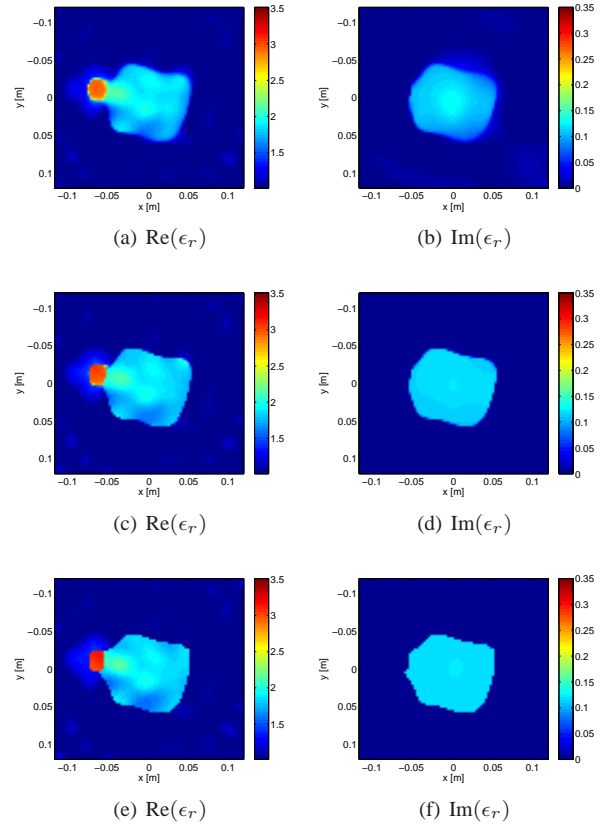
be noted that the sensitivity of the quantitative accuracy of the reconstructed image is low with respect to Q and $Q_{TV} = Q$ when they change from 10 to 40.

The final data misfit value $\tilde{\mathcal{C}}^{LS}$ for the MR-GNI algorithm is $\approx 0.2\%$, for the PSMR-GNI with Q and Q_{TV} both equal to 10, 20, 40, and 60, it is $\approx 0.1\%$. It should be noted that a smaller data misfit cost-functional does not necessarily mean a better reconstruction due to the ill-posedness of the MWT problem.

We next consider the target shown in Fig. 3(a) and (b). The right-most detail of this target has a relative complex permittivity of $33 + j5$ and the rest of the target has a relative complex permittivity of $33 + j1.2$. The relative complex permittivity of the background medium is $23 + j$. That is, the target consists of two different contrasts: $0.44 + j0.15$ and $0.43 - j0.01$. As opposed to the first synthetic case where there was only one ratio between the real and imaginary parts of the contrast, this target consists of two different contrasts with two completely different ratios between the real and imaginary parts: the ratio between the real and imaginary parts of the contrast is about 3 in the right-most detail of the target and is about 40 in the rest of the target. For this target, the true Q is about 13 whereas the true numerical Q_{TV} is about 10. The noisy synthetic data at $f = 2$ GHz is collected using the same procedure used for the first synthetic data set as is the discretized imaging domain. The MR-GNI reconstruction
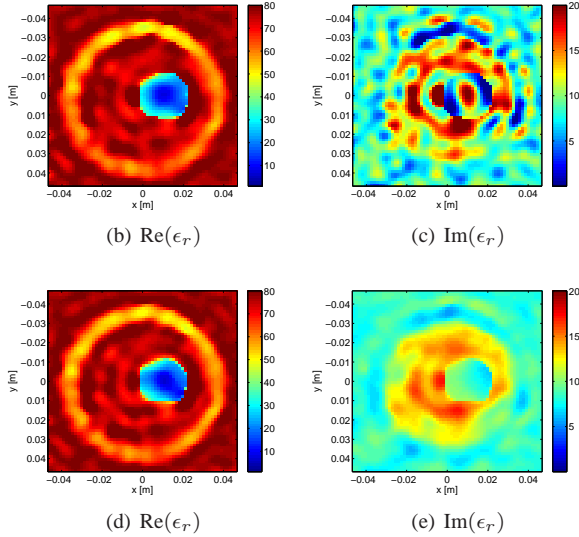
(a) FANTCENT phantom

(b) Re(ϵ_r)

(c) Im(ϵ_r)

(d) Re(ϵ_r)

(e) Im(ϵ_r)
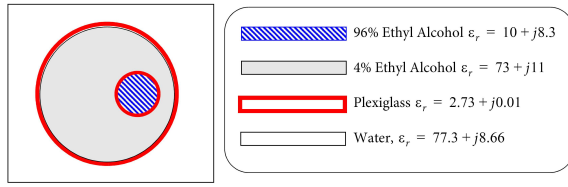
Fig. 7.   (a) FANTCENT phantom, (c)-(d) its reconstruction using MR-GNI, (e)-(f) its reconstruction using PSMR-GNI with $Q = Q_{\text{TV}} = 5$.

(a) Re(ϵ_r)

(b) Im(ϵ_r)

(c) Re(ϵ_r)

(d) Im(ϵ_r)

(e) Re(ϵ_r)

(f) Im(ϵ_r)

Fig. 8.   The reconstructed relative complex permittivity of the FANTCENT phantom using (a)-(b) PSMR-GNI with $Q = Q_{\text{TV}} = 10$, (c)-(d) PSMR-GNI with $Q = Q_{\text{TV}} = 20$, and (e)-(f) PSMR-GNI with $Q = 3$ and $Q_{\text{TV}} = 5$.

of this target is shown in Fig. 3(c) and (d). As can be seen, the imaginary part of the contrast is very oscillatory. Using the PSMR-GNI method with $Q = Q_{\text{TV}} = 5$, both real- and imaginary-part reconstructions of the target are shown in Fig. 3(e) and (f). Except for undershooting the imaginary-part of the right-most detail, the reconstruction is satisfactory. The inversion results using the PSMR-GNI method with $Q = Q_{\text{TV}} = 10$ and $Q = Q_{\text{TV}} = 13$ are shown in Fig. 4(a)-(d). As can be seen, the inversion results using $Q = Q_{\text{TV}} = 10$ and $Q = Q_{\text{TV}} = 13$ are very similar to the inversion results using $Q = Q_{\text{TV}} = 5$. However, the pre-scaled inversion begins to deteriorate at $Q = Q_{\text{TV}} = 20$. We have also utilized the true values for Q and Q_{TV} in the inversion algorithm which resulted in a very similar reconstruction as the case where $Q = Q_{\text{TV}} = 10$. That the reconstructed imaginary part of the rightmost detail of the target undershoots its true value and that the separation between the two rightmost details of the target has not been resolved in the reconstructed imaginary part is probably due to the fact the pre-scaled inversion algorithm provides an over-regularized reconstruction for that region of the target. However, it provides a reasonable regularization weight for the rest of the target. We note that the standard MR-GNI method provides an under-regularized reconstruction for the whole imaginary part of the target.

Finally, we remark that we have also inverted these two synthetic data sets using the multiplicative-regularized contrast source inversion (MR-CSI) algorithm as outlined in [3]. The inversion results using the MR-CSI method were very similar
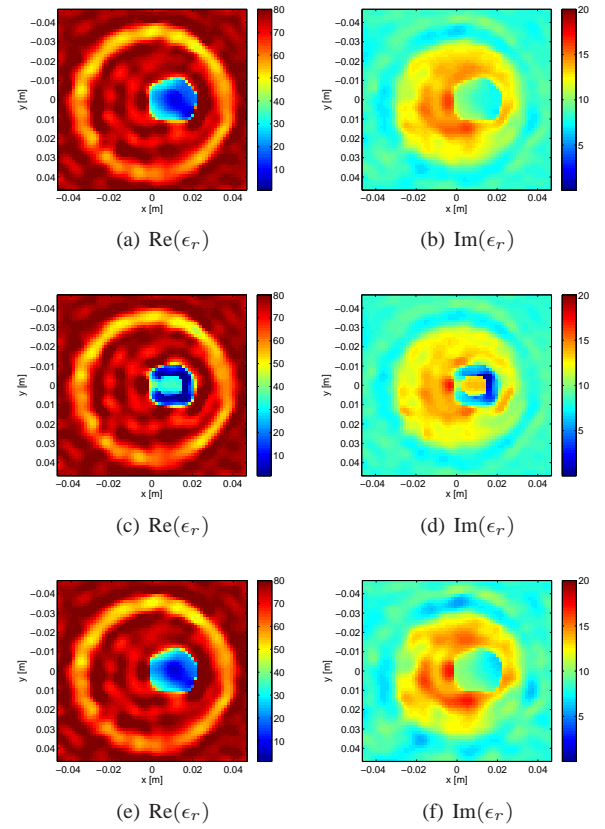
to the inversion results using the standard MR-GNI method.

VI. EXPERIMENTAL DATA RESULTS

We consider two different MWT systems. The first system is the University of Manitoba air-filled MWT system [28] which utilizes 24 co-resident Vivaldi antennas capable of collecting data from 3 GHz to 6 GHz. The single-frequency measured data, which consists of 24×23 measurements, is calibrated for the TM polarization as explained in [28]. In this work, we choose the frequency of operation to be 3 GHz for this system. The second system is the Universitat Politècnica de Catalunya (UPC) MWT system. This system is a near-field 2.33 GHz microwave scanner system which consists of 64 water-immersed antennas equispaced on a 12.5 cm-radius circular array [29]. In this system, for each case of using one of the 64 antennas as a sole transmitter, field data is collected using only the 33 antennas positioned in front of the transmitting antenna. The measured data is then calibrated for the TM polarization.

1) Wood-Nylon Data Set: We utilize a circular nylon-66 cylinder with a diameter of 3.8 cm and an (approximately) square cross-section wooden block with the side of 0.087 m. The complex relative permittivities of wood and nylon are $\epsilon_r^{\text{wood}} \approx 2.0 + j0.2$ and $\epsilon_r^{\text{nylon}} \approx 3.0 + j0.03$ at 3 GHz, respectively [28]. Thus, the ratio between the real and imaginary parts of the *contrast* is about 5 in wood and 67 in the nylon

rod. In addition, noting the structure of the target, it is expected that the true numerical Q_{TV} be close to the true Q. The target was placed in the University of Manitoba MWT system as shown in Fig. 5(a). The inversion result using the MR-GNI method is shown in Fig. 5(b) and (c). As can be seen, the imaginary-part reconstruction is not satisfactory. Using the PSMR-GNI method with $Q = Q_{\mathrm{TV}} = 10$, see Fig. 5(d) and (e), both real- and imaginary-part reconstructions are satisfactory: the reconstructed imaginary part is not oscillatory and the reconstructed value for the real part of the nylon rod is more accurate compared to its reconstructed value using the MR-GNI method. The reconstructed imaginary part of wood using the PSMR-GNI method is about 0.12 which undershoots its true value. We note that the nylon rod is almost lossless; thus, it is very difficult to reconstruct its imaginary part considering the limited signal-to-noise ratio and dynamic range of the system. The inversion results using the PSMR-GNI method for three more values of Q and Q_{TV}; namely $Q = Q_{\mathrm{TV}} = 20$, $Q = Q_{\mathrm{TV}} = 40$, and $Q = Q_{\mathrm{TV}} = 70$ are shown in Fig. 6. It is worth mentioning that the MR-CSI reconstruction of this target, which has been shown in [28], also results in a non-satisfactory imaginary-part reconstruction.

2) FANTCENT Data Set: We next consider the FANT-CENT phantom from the UPC Barcelona experimental data set which is shown in Fig. 7(a). The phantom consists of two thin plexiglass cylinders filled with two different concentrations of ethyl alcohol. The inversion results are constrained to lie within the region defined by $0 \leq \mathrm{Re}(\epsilon_r) \leq 80$ and $0 \leq \mathrm{Im}(\epsilon_r) \leq 20$, as in [3]. The MR-GNI inversion of this data set is shown in Fig. 7(b) and (c). Although the real-part reconstruction is satisfactory, the imaginary-part reconstruction is very oscillatory. The PSMR-GNI reconstructions with four different values for Q and Q_{TV} are shown in Fig. 7(d) and (e) and Fig. 8. As can be seen, having Q equal to 5 and 10 and choosing Q_{TV} to be the same as Q improves the imaginary-part reconstruction compared to the MR-GNI reconstruction. However, increasing Q and Q_{TV} to 20 starts deteriorating the reconstruction. This is probably due to the fact that $Q = Q_{\mathrm{TV}} = 20$ provides an over-regularized solution. We note that the ratio between the real and imaginary parts of the contrast is about 9.5 in 96% ethyl alcohol and 1.7 in 4% ethyl alcohol. The thickness of the two plexiglass cylinders are too small to be reconstructed (2 mm thickness for the outer cylinder and 1.5 mm for the inner cylinder); thus, we have not used the ratio between the real and imaginary parts of the plexiglass contrast in the PSMR-GNI algorithm. Having created a *numerical* phantom similar to the FANTCENT phantom, but excluding the plexiglass containers, we have found the true value of Q to be 3 and the true value of Q_{TV} to be 5. The PSMR-GNI reconstruction for these two values of Q and Q_{TV} are shown in Fig. 8(e) and (f). Finally, we note that the MR-CSI reconstruction of this target, shown in [3], provides a good overall reconstruction for both real and imaginary parts of the phantom. However, the PSMR-GNI algorithm provides a slightly more accurate quantitative reconstruction for the 4% ethyl alcohol. It should also be noted that in all the examples we have tried, the quantitative accuracy of the reconstructed image was not very sensitive to the values of Q and Q_{TV}.

VII. CONCLUSION

We have shown that the PSMR-GNI can provide a good reconstruction for both real and imaginary parts of the relative complex permittivity when there is a large imbalance between the real and imaginary parts of the OI's electric contrast. It has also been demonstrated that the PSMR-GNI is not very sensitive to the choice of the pre-scaling parameters.

APPENDIX

The required derivative operators in the continuous domain are derived and then presented in their discretized forms. We denote the L_2 spaces of complex functions defined on $\mathcal{D}$ and $\mathcal{S}$ by $L_2(\mathcal{D})$ and $L_2(\mathcal{S})$ with the norms and inner products defined as

$$\|\psi\|_{\mathcal{D}} = \langle \psi, \psi \rangle_{\mathcal{D}}^{1/2} \quad \text{and} \quad \langle \psi, \varphi \rangle_{\mathcal{D}} = \int_{\mathcal{D}} \psi(\boldsymbol{q}) \varphi^*(\boldsymbol{q}) d\boldsymbol{q} \quad (17)$$

and

$$\|Y\|_{\mathcal{S}} = \langle Y, Y \rangle_{\mathcal{S}}^{1/2} \quad \text{and} \quad \langle Y_1, Y_2 \rangle_{\mathcal{S}} = \int_{\mathcal{S}} Y_1(\boldsymbol{p}) Y_2^*(\boldsymbol{p}) d\boldsymbol{p} \quad (18)$$

where the superscript $*$ denotes the complex conjugate operator.

To find the derivative operators of the data misfit cost-functional $\tilde{\mathcal{C}}^{\mathrm{LS}}(\chi_{\mathrm{R}}, \chi_{\mathrm{I}})$ with respect to χ_{R} and χ_{I} at the nth iteration, we start by finding the Gâteaux differential of $\mathcal{C}^{\mathrm{LS}}$ in the ψ direction [30, pg. 468]

$$d\mathcal{C}^{\mathrm{LS}}(\chi_n, \psi) = \lim_{\epsilon \to 0} \frac{\mathcal{C}^{\mathrm{LS}}(\chi_n + \epsilon \psi) - \mathcal{C}^{\mathrm{LS}}(\chi_n)}{\epsilon} \quad (19)$$

where $\epsilon \in \mathbb{R}$ and ψ is an arbitrary complex function which belongs to $L_2(\mathcal{D})$. Utilizing the little-o notation, $\lim_{\|\psi\|_{\mathcal{D}} \to 0} \frac{o(\|\psi\|_{\mathcal{D}})}{\|\psi\|_{\mathcal{D}}} = 0$, expression (19) can be written as

$$\lim_{\epsilon \to 0} \frac{\eta_{\mathcal{S}}}{\epsilon} \left[\sum_{t=1}^{T_x} \left\| E_t^{\mathrm{scat}}(\chi_n) + \epsilon \frac{\partial E_t^{\mathrm{scat}}}{\partial \chi} \Big|_{\chi_n} (\psi) + o(\|\epsilon \psi\|_{\mathcal{D}}) - E_{\mathrm{meas},t}^{\mathrm{scat}} \right\|_{\mathcal{S}}^2 \right.$$
$$\left. - \sum_{t=1}^{T_x} \left\| E_t^{\mathrm{scat}}(\chi_n) - E_{\mathrm{meas},t}^{\mathrm{scat}} \right\|_{\mathcal{S}}^2 \right] \quad (20)$$

and simplified to

$$2\eta_{\mathcal{S}} \sum_{t=1}^{T_x} \mathrm{Re} \left\langle E_t^{\mathrm{scat}}(\chi_n) - E_{\mathrm{meas},t}^{\mathrm{scat}}, \frac{\partial E_t^{\mathrm{scat}}}{\partial \chi} \Big|_{\chi_n} (\psi) \right\rangle_{\mathcal{S}}. \quad (21)$$

Denoting the adjoint operator by the superscript 'a', (21) may be written as

$$\mathrm{Re} \left\langle 2\eta_{\mathcal{S}} \sum_{t=1}^{T_x} \left[\frac{\partial E_t^{\mathrm{scat}}}{\partial \chi} \Big|_{\chi_n} \right]^a \left(E_t^{\mathrm{scat}}(\chi_n) - E_{\mathrm{meas},t}^{\mathrm{scat}} \right), \psi \right\rangle_{\mathcal{D}}, \quad (22)$$

where now the inner product is on $\mathcal{D}$. For two complex functions, φ and ψ, we have

$$\mathrm{Re} \langle \varphi, \psi \rangle_{\mathcal{D}} = \langle \varphi_{\mathrm{R}}, \psi_{\mathrm{R}} \rangle_{\mathcal{D}} + \langle \varphi_{\mathrm{I}}, \psi_{\mathrm{I}} \rangle_{\mathcal{D}}. \quad (23)$$

Thus, (22) may be written as

$$
\left\langle 2\eta_S \sum_{t=1}^{T_x} \text{Re} \left\{ \left[\frac{\partial E_t^{\text{scat}}}{\partial \chi} \Big|_{\chi_n} \right]^a \left(E_t^{\text{scat}}(\chi) - E_{\text{meas},t}^{\text{scat}} \right) \right\}, \psi_R \right\rangle_{\mathcal{D}} +
$$

$$
\left\langle 2\eta_S \sum_{t=1}^{T_x} \text{Im} \left\{ \left[\frac{\partial E_t^{\text{scat}}}{\partial \chi} \Big|_{\chi_n} \right]^a \left(E_t^{\text{scat}}(\chi) - E_{\text{meas},t}^{\text{scat}} \right) \right\}, \psi_I \right\rangle_{\mathcal{D}}. \quad (24)
$$

The first term of (24) represents $\frac{\partial \tilde{\mathcal{C}}^{\text{LS}}}{\partial \chi_R} \Big|_{\chi_n} (\psi_R)$ and the second term represents $\frac{\partial \tilde{\mathcal{C}}^{\text{LS}}}{\partial \chi_I} \Big|_{\chi_n} (\psi_I)$. We note that these derivative operators are linear mappings from $L_2(\mathcal{D})$ to $\mathbb{R}$.

To find the second derivatives $\left[\frac{\partial^2 \tilde{\mathcal{C}}^{\text{LS}}}{\partial \chi_R \partial \chi_I} |_{\chi_n}(\varphi_I) \right] (\psi_R)$ and $\left[\frac{\partial^2 \tilde{\mathcal{C}}^{\text{LS}}}{\partial \chi_I \partial \chi_I} |_{\chi_n}(\varphi_I) \right] (\psi_I)$ at the nth iteration of the inversion algorithm, we start with finding the limit

$$
\lim_{\epsilon \to 0} \frac{\frac{\partial \tilde{\mathcal{C}}^{\text{LS}}}{\partial \chi_I} |_{\chi_n + \epsilon \psi}(\varphi_I) - \frac{\partial \tilde{\mathcal{C}}^{\text{LS}}}{\partial \chi_I} |_{\chi_n}(\varphi_I)}{\epsilon}. \quad (25)
$$

Utilizing the operators just calculated, and the definition of the adjoint operator, the above limit may be written as

$$
\lim_{\epsilon \to 0} \frac{2\eta_S}{\epsilon} \sum_{t=1}^{T_x} \left[\text{Im} \left\langle E_t^{\text{scat}}(\chi_n + \epsilon \psi) - E_{\text{meas},t}^{\text{scat}}, \frac{\partial E_t^{\text{scat}}}{\partial \chi} \Big|_{\chi_n + \epsilon \psi}(\varphi_I) \right\rangle_{\mathcal{D}} \right.
$$

$$
\left. - \text{Im} \left\langle E_t^{\text{scat}}(\chi_n) - E_{\text{meas},t}^{\text{scat}}, \frac{\partial E_t^{\text{scat}}}{\partial \chi} |_{\chi_n}(\varphi_I) \right\rangle_{\mathcal{D}} \right]. \quad (26)
$$

This can be simplified to

$$
2\eta_S \sum_{t=1}^{T_x} \left[- \text{Im} \left\langle \left[\frac{\partial E_t^{\text{scat}}}{\partial \chi} |_{\chi_n} \right]^a \left[\frac{\partial E_t^{\text{scat}}}{\partial \chi} |_{\chi_n} \right](\varphi_I), \psi \right\rangle_{\mathcal{D}} + \right.
$$

$$
\left. \text{Im} \left\langle \left[\frac{\partial^2 E_t^{\text{scat}}}{\partial \chi^2} |_{\chi_n}(\varphi_I) \right]^a (E_t^{\text{scat}}(\chi_n) - E_{\text{meas},t}^{\text{scat}}), \psi \right\rangle_{\mathcal{D}} \right]. \quad (27)
$$

Noting that for two complex functions, φ and ψ, we have

$$
\text{Im} \langle \varphi, \psi \rangle_{\mathcal{D}} = \langle \varphi_I, \psi_R \rangle_{\mathcal{D}} - \langle \varphi_R, \psi_I \rangle_{\mathcal{D}}, \quad (28)
$$

expression (27) may be written as

$$
2\eta_S \sum_{t=1}^{T_x} \left[\left\langle - \text{Im} \left\{ \left[\frac{\partial E_t^{\text{scat}}}{\partial \chi} \Big|_{\chi_n} \right]^a \left[\frac{\partial E_t^{\text{scat}}}{\partial \chi} |_{\chi_n} \right](\varphi_I) \right\}, \psi_R \right\rangle_{\mathcal{D}} + \right.
$$

$$
\left\langle \text{Re} \left\{ \left[\frac{\partial E_t^{\text{scat}}}{\partial \chi} \Big|_{\chi_n} \right]^a \left[\frac{\partial E_t^{\text{scat}}}{\partial \chi} |_{\chi_n} \right](\varphi_I) \right\}, \psi_I \right\rangle_{\mathcal{D}} +
$$

$$
\left\langle \text{Im} \left\{ \left[\frac{\partial^2 E_t^{\text{scat}}}{\partial \chi^2} \Big|_{\chi_n}(\varphi_I) \right]^a (E_t^{\text{scat}}(\chi_n) - E_{\text{meas},t}^{\text{scat}}) \right\}, \psi_R \right\rangle_{\mathcal{D}} -
$$

$$
\left. \left\langle \text{Re} \left\{ \left[\frac{\partial^2 E_t^{\text{scat}}}{\partial \chi^2} \Big|_{\chi_n}(\varphi_I) \right]^a (E_t^{\text{scat}}(\chi_n) - E_{\text{meas},t}^{\text{scat}}) \right\}, \psi_I \right\rangle_{\mathcal{D}} \right] \quad (29)
$$

Therefore,

$$
\frac{\partial^2 \tilde{\mathcal{C}}^{\text{LS}}}{\partial \chi_R \partial \chi_I} \Big|_{\chi_n} (\varphi_I)(\psi_R) =
$$

$$
\left\langle 2\eta_S \sum_{t=1}^{T_x} \text{Im} \left\{ - \left[\frac{\partial \mathcal{E}_t^{\text{scat}}}{\partial \chi} \Big|_{\chi_n} \right]^a \left[\frac{\partial \mathcal{E}_t^{\text{scat}}}{\partial \chi} \Big|_{\chi_n} \right](\varphi_I) + \right. \right.
$$

$$
\left. \left. \left[\frac{\partial^2 \mathcal{E}_t^{\text{scat}}}{\partial \chi^2} \Big|_{\chi_n}(\varphi_I) \right]^a (E_t^{\text{scat}}(\chi_n) - E_{\text{meas},t}^{\text{scat}}) \right\}, \psi_R \right\rangle_{\mathcal{D}} \quad (30)
$$

and

$$
\frac{\partial^2 \tilde{\mathcal{C}}^{\text{LS}}}{\partial \chi_I \partial \chi_I} \Big|_{\chi_n} (\varphi_I)(\psi_I) =
$$

$$
\left\langle 2\eta_S \sum_{t=1}^{T_x} \text{Re} \left\{ \left[\frac{\partial E_t^{\text{scat}}}{\partial \chi} \Big|_{\chi_n} \right]^a \left[\frac{\partial E_t^{\text{scat}}}{\partial \chi} \Big|_{\chi_n} \right](\varphi_I) - \right. \right.
$$

$$
\left. \left. \left[\frac{\partial^2 E_t^{\text{scat}}}{\partial \chi^2} \Big|_{\chi_n}(\varphi_I) \right]^a (E_t^{\text{scat}}(\chi_n) - E_{\text{meas},t}^{\text{scat}}) \right\}, \psi_I \right\rangle_{\mathcal{D}}. \quad (31)
$$

To find the derivatives $\left[\frac{\partial^2 \tilde{\mathcal{C}}^{\text{LS}}}{\partial \chi_I \partial \chi_R} |_{\chi_n}(\varphi_R) \right] (\psi_I)$ and $\left[\frac{\partial^2 \tilde{\mathcal{C}}^{\text{LS}}}{\partial \chi_R \partial \chi_R} |_{\chi_n}(\varphi_R) \right] (\psi_R)$, we start with finding the limit

$$
\lim_{\epsilon \to 0} \frac{\frac{\partial \tilde{\mathcal{C}}^{\text{LS}}}{\partial \chi_R} |_{\chi = \chi_n + \epsilon \psi}(\varphi_R) - \frac{\partial \tilde{\mathcal{C}}^{\text{LS}}}{\partial \chi_R} |_{\chi = \chi_n}(\varphi_R)}{\epsilon}. \quad (32)
$$

After mathematical simplifications similar to the ones presented above, the limit (32) will be

$$
2\eta_S \sum_{t=1}^{T_x} \left[\text{Re} \left\langle \left[\frac{\partial E_t^{\text{scat}}}{\partial \chi} \Big|_{\chi_n} \right]^a \left[\frac{\partial E_t^{\text{scat}}}{\partial \chi} \Big|_{\chi_n} \right](\varphi_R), \psi \right\rangle_{\mathcal{D}} + \right.
$$

$$
\left. \text{Re} \left\langle \left[\frac{\partial^2 E_t^{\text{scat}}}{\partial \chi^2} \Big|_{\chi_n}(\varphi_R) \right]^a (E_t^{\text{scat}}(\chi_n) - E_{\text{meas},t}^{\text{scat}}), \psi \right\rangle_{\mathcal{D}} \right]. \quad (33)
$$

Noting (33) and utilizing (23), it can be concluded that

$$
\frac{\partial^2 \tilde{\mathcal{C}}^{\text{LS}}}{\partial \chi_I \partial \chi_R} \Big|_{\chi_n} (\varphi_R)(\psi_I) =
$$

$$
\left\langle 2\eta_S \sum_{t=1}^{T_x} \text{Im} \left\{ \left[\frac{\partial E_t^{\text{scat}}}{\partial \chi} \Big|_{\chi_n} \right]^a \left[\frac{\partial E_t^{\text{scat}}}{\partial \chi} |_{\chi_n} \right](\varphi_R) + \right. \right.
$$

$$
\left. \left. \left[\frac{\partial^2 E_t^{\text{scat}}}{\partial \chi^2} \Big|_{\chi_n}(\varphi_R) \right]^a (E_t^{\text{scat}}(\chi_n) - E_{\text{meas},t}^{\text{scat}}) \right\}, \psi_I \right\rangle_{\mathcal{D}} \quad (34)
$$

and

$$
\frac{\partial^2 \tilde{\mathcal{C}}^{\text{LS}}}{\partial \chi_R \partial \chi_R} \Big|_{\chi_n} (\varphi_R)(\psi_R) =
$$

$$
\left\langle 2\eta_S \sum_{t=1}^{T_x} \text{Re} \left\{ \left[\frac{\partial E_t^{\text{scat}}}{\partial \chi} \Big|_{\chi_n} \right]^a \left[\frac{\partial E_t^{\text{scat}}}{\partial \chi} \Big|_{\chi_n} \right](\varphi_R) + \right. \right.
$$

$$
\left. \left. \left[\frac{\partial^2 E_t^{\text{scat}}}{\partial \chi^2} \Big|_{\chi_n}(\varphi_R) \right]^a (E_t^{\text{scat}}(\chi_n) - E_{\text{meas},t}^{\text{scat}}) \right\}, \psi_R \right\rangle_{\mathcal{D}}. \quad (35)
$$

The second-order derivative operators in (30), (31), (34), and (35), are linear mappings from $L_2(\mathcal{D}) \times L_2(\mathcal{D})$ to $\mathbb{R}$. It should also be noted that in the Gauss-Newton inversion method, the operator $\partial^2 E_t^{\text{scat}}/\partial \chi^2$ is neglected and thus (30), (31), (34), and (35) are simplified.

The PSMR-GNI method also requires the derivatives of $\mathcal{C}_n^{\text{PSMR}}$ with respect to χ_R and χ_I. Using the same procedure explained above, these derivatives can be derived. The closed-form expressions of these derivative operators are given in [31, Appendix D].

Having found the derivative operators in the continuous domain, the discretized forms of these operators can easily be found. For example, the discretized form of $\frac{\partial \tilde{\mathcal{C}}^{\text{LS}}}{\partial \chi_R} \Big|_{\chi_n} (\psi_R)$ can be written as

$$
\left[\frac{\partial \tilde{\mathcal{C}}^{\text{LS}}}{\partial \underline{\chi}_R} \Big|_{\underline{\chi}_n} \right]^T \underline{\psi}_R = \left[- 2\eta_S \text{Re} \left\{ \underline{\boldsymbol{J}}_n^H \underline{d}_n \right\} \right]^T \underline{\psi}_R \quad (36)
$$

where the superscript 'T' denotes the transposition operator. As another example, the discretized form of (35), calculated under the GNI approximation, can be expressed as

$$
\left[\frac{\partial^2 \tilde{\mathcal{C}}^{\mathrm{LS}}}{\partial \underline{\chi}_{\mathrm{R}} \partial \underline{\chi}_{\mathrm{R}}} \bigg|_{\underline{\chi}_n} \underline{\varphi}_{\mathrm{R}} \right]^T \underline{\psi}_{\mathrm{R}} \approx \left[2\eta_{\mathcal{S}} \mathrm{Re} \left\{ \underline{\boldsymbol{J}}_n^H \underline{\boldsymbol{J}}_n \right\} \underline{\varphi}_{\mathrm{R}} \right]^T \underline{\psi}_{\mathrm{R}} \quad (37)
$$

REFERENCES

[1] P. M. van den Berg and R. E. Kleinman, "A contrast source inversion method," *Inverse Probl.*, vol. 13, pp. 1607–1620, 1997.

[2] A. Abubakar, W. Hu, P. van den Berg, and T. Habashy, "A finite-difference contrast source inversion method," *Inverse Problems*, vol. 24, p. 065004 (17pp), 2008.

[3] A. Abubakar, P. M. van den Berg, and J. J. Mallorqui, "Imaging of biomedical data using a multiplicative regularized contrast source inversion method," *IEEE Trans. Microwave Theory Tech.*, vol. 50, no. 7, pp. 1761–1777, July 2002.

[4] C. Gilmore, P. Mojabi, and J. LoVetri, "Comparison of an enhanced distorted Born iterative method and the multiplicative-regularized contrast source inversion method," *IEEE Trans. Antennas Propag.*, vol. 57, no. 8, pp. 2341–2351, Aug. 2009.

[5] P. Mojabi and J. LoVetri, "Eigenfunction contrast source inversion for circular metallic enclosures," *Inverse Problems*, vol. 26, no. 2, Feb. 2010, 025010 (23pp).

[6] A. Zakaria, C. Gilmore, and J. LoVetri, "Finite-element contrast source inversion method for microwave imaging," *Inverse Problems*, vol. 26, no. 11, 2010, 115010 (21pp).

[7] T. M. Habashy and A. Abubakar, "A general framework for constraint minimization for the inversion of electromagnetic measurements," *Progress in Electromagnetics Research*, vol. 46, pp. 265–312, 2004.

[8] W. C. Chew and Y. M. Wang, "Reconstruction of two-dimensional permittivity distribution using the distorted Born iterative method," *IEEE Trans. Med. Imaging*, vol. 9, no. 2, pp. 218–225, 1990.

[9] A. Abubakar, T. Habashy, V. Druskin, L. Knizhnerman, and D. Alumbaugh, "2.5D forward and inverse modeling for interpreting low-frequency electromagnetic measurements," *Geophysics*, vol. 73, no. 4, pp. F165–F177, July-Aug 2008.

[10] P. Mojabi and J. LoVetri, "Microwave biomedical imaging using the multiplicative regularized Gauss–Newton inversion," *IEEE Antennas and Wireless Propagation Letters*, vol. 8, pp. 645–648, 2009.

[11] J. D. Zaeytijd, A. Franchois, C. Eyraud, and J.-M. Geffrin, "Full-wave three-dimensional microwave imaging with a regularized Gauss-Newton method–theory and experiment," *IEEE Trans. Antennas Propag.*, vol. 55, no. 11, pp. 3279–3292, Nov 2007.

[12] M. Pastorino, "Stochastic optimization methods applied to microwave imaging: A review," *IEEE Trans. Antennas Propag.*, vol. 55, no. 3, pp. 538–548, March 2007.

[13] L. Garnero, A. Franchois, J. P. Hugonin, C. Pichot, and N. Joachimowicz, "Microwave imaging–complex permittivity reconstruction by simulated annealing," *IEEE Trans. Microw. Theory Tech.*, vol. 39, no. 11, pp. 1801–1807, Nov 1991.

[14] S. Caorsi, A. Massa, and M. A. Pastorino, "A computational technique based on a real-coded genetic algorithm for microwave imaging purposes," *IEEE Trans. Geosci. Remote Sensing*, vol. 38, no. 4, pp. 1697–1708, 2000.

[15] A. E. Bulyshev, A. E. Souvorov, S. Y. Semenov, R. H. Svenson, A. G. Nazarov, Y. E. Sizov, and G. P. Tastis, "Three dimensional microwave tomography. theory and computer experiments in scalar approximation," *Inverse Probl.*, vol. 16, pp. 863–875, 2000.

[16] A. E. Bulyshev, A. E. Souvorov, S. Y. Semenov, V. G. Posukh, and Y. E. Sizov, "Three dimensional vector microwave tomography: Theory and computational experiments," *Inverse Probl.*, vol. 20, pp. 1239–1259, 2004.

[17] T. Rubæk, P. M. Meaney, P. Meincke, and K. D. Paulsen, "Nonlinear microwave imaging for breast-cancer screening using Gauss-Newton's method and the CGLS inversion algorithm," *IEEE Trans. Antennas Propag.*, vol. 55, no. 8, pp. 2320–2331, Aug 2007.

[18] P. Mojabi and J. LoVetri, "Enhancement of the Krylov subspace regularization for microwave biomedical imaging," *IEEE Trans. Med. Imag.*, vol. 28, no. 12, pp. 2015–2019, Dec. 2009.

[19] Z. Wu, H. McCann, L. E. Davis, J. Hu, A. Fontes, and C. G. Xie, "Microwave-tomographic system for oil- and gas-multiphase-flow imaging," *Measurement Science and Technology*, vol. 20, no. 10, p. 104026, 2009. [Online]. Available: http://stacks.iop.org/0957-0233/20/i=10/a=104026

[20] S. Semenov, "Microwave tomography: review of the progress towards clinical applications," *Phil. Trans. R. Soc. A*, vol. 367, pp. 3021–3042, July 2009.

[21] P. M. Meaney, M. W. Fanning, T. Raynolds, C. J. Fox., Q. Fang, C. A. Kogel, S. P. Poplack, and K. D. Paulsen, "Initial clinical experience with microwave breast imaging in women with normal mammography," *Acad Radiol.*, March 2007.

[22] S. Poplack, T. Tosteson, W. Wells, B. Pogue, P. Meaney, A. Hartov, C. Kogel, S. Soho, J. Gibson, and K. Paulsen, "Electromagnetic breast imaging results of a pilot study in women with abnormal mammograms," *Radiology*, vol. 243, no. 2, pp. 350–359, 2007.

[23] P. Meaney, N. Yagnamurthy, and K. D. Paulsen, "Pre-scaled two-parameter Gauss-Newton image reconstruction to reduce property recovery imbalance," *Phys. Med. Biol.*, vol. 47, pp. 1101–1119, 2002.

[24] P. Mojabi and J. LoVetri, "Overview and classification of some regularization techniques for the Gauss-Newton inversion method applied to inverse scattering problems," *IEEE Trans. Antennas Propag.*, vol. 57, no. 9, pp. 2658–2665, Sept. 2009.

[25] S. Semenov, R. Svenson, A. Bulyshev, A. Souvorov, A. Nazarov, Y. Sizov, V. Posukh, A. Pavlovsky, P. Repin, and G. Tatsis, "Spatial resolution of microwave tomography for detection of myocardial ischemia and infarction-experimental study on two-dimensional models," *IEEE Trans. Microwave Theory Tech.*, vol. 48, no. 4, pp. 538–544, Apr 2000.

[26] C. Gilmore, P. Mojabi, A. Zakaria, S. Pistorius, and J. LoVetri, "On super-resolution with an experimental microwave tomography system," *IEEE Antennas and Wireless Propagation Letters*, vol. 9, pp. 393–396, 2010.

[27] A. Abubakar, P. M. van den Berg, and S. Y. Semenov, "A robust iterative method for Born inversion," *IEEE Trans. Geosci. Remote Sensing*, vol. 42, no. 2, pp. 342–354, Feb 2004.

[28] C. Gilmore, P. Mojabi, A. Zakaria, M. Ostadrahimi, C. Kaye, S. Noghanian, L. Shafai, S. Pistorius, and J. LoVetri, "A wideband microwave tomography system with a novel frequency selection procedure," *IEEE Trans. Biomed. Eng.*, vol. 57, no. 4, pp. 894–904, April 2010.

[29] A. Broquetas, J. Romeu, J. Rius, A. Elias-Fuste, A. Cardama, and L. Jofre, "Cylindrical geometry: a further step in active microwave tomography," *IEEE Trans. Microwave Theory Tech.*, vol. 39, no. 5, pp. 836–844, May 1991.

[30] L. Debnath and P. Mikusiński, *Introduction to Hilbert Spaces with Applications*. Burlington, MA: Elsevier Academic Press, 2005.

[31] P. Mojabi, "Investigation and development of algorithms and techniques for microwave tomography," Ph.D. dissertation, University of Manitoba, Winnipeg, Manitoba, Canada, 2010, URL: http://mspace.lib.umanitoba.ca/handle/1993/3946.